catalysts

MDPI

Article

CO_2 Oxidative Dehydrogenation of Propane to Olefin over Cr-M (M = Zr, La, Fe) Based Zeolite Catalyst

Mingqiao Xing, Ning Liu *, Chengna Dai and Biaohua Chen

College of Environmental Science and Engineering, Beijing University of Technology, Beijing 100124, China; xmqiao@emails.bjut.edu.cn (M.X.); daicn@bjut.edu.cn (C.D.); chenbh@bjut.edu.cn (B.C.)
* Correspondence: liuning@bjut.edu.cn

Abstract: CO_2 oxidative dehydrogenation of propane (CO_2-ODHP), being not only favorable for olefin production but also beneficial for CO_2 emission control, has recently attracted great attention. Here, a series of single metal (Cr) and bimetal (Zr, La, Fe) modified ZSM-5 zeolites were prepared via an impregnation method. It was found that the bimetal modified ZSM-5 possessed much higher C_3H_8 and CO_2 conversion than that of monometallic modified $Cr_{3\%}$-ZSM-5 ($Cr_{3\%}$-Z5), especially for $Cr_{3\%}Zr_{2\%}$-ZSM-5 ($Cr_{3\%}Zr_{2\%}$-Z5), which displayed the highest activity (65.4%) and olefin yield (1.65×10^3 μmol·g_{cat}^{-1} h^{-1}). Various characterizations were performed, including XRD, N_2 adsorption-desorption, H_2-TPR, Raman, XPS, HAAD-STEM, and TEM. It was revealed that Zr not only favored an improvement in the redox ability of Cr, but also contributed to the surface dispersion of loaded Cr species, constituting two major reasons explaining the superior activity of $Cr_{3\%}Zr_{2\%}$-Z5. To further improve CO_2-ODHP catalytic behavior, a series of $Cr_{3\%}$-ZSM-5@SBA-15-n composite zeolite catalysts with diverse (ZSM-5/SBA-15) mass ratios were prepared ($Cr_{3\%}$-ZS-n, n = 0.5, 2, 6, 16), which screened out an optimum mass ratio of six. Based on this, the $Cr_{3\%}Zr_{2\%}$-ZS-6 compound was further prepared, and it eventually achieved even higher CO_2-ODHP activity (76.9%) and olefin yield (1.72×10^3 μmol·g_{cat}^{-1} h^{-1}). Finally, the CO_2-ODHP reaction mechanism was further investigated using in situ FTIR, and it was found that the reaction followed the Mars–van Krevelen mechanism, wherein CO_2 participated in the reaction through generation of polydentate carbonates. The Cr^{6+} constituted as the active site, which was reduced to Cr^{3+} after the dihydrogen reaction, and was then further oxidized into Cr^{6+} by CO_2, forming polydentate carbonates, and thus cycling the reactive species Cr^{6+}. Additionally, assisted by a Brönsted acid site (favoring breaking of the C-C bond), C_2H_4 and CH_4 were produced.

Keywords: propane oxidative to olefin; CO_2; molecular sieve catalysts; chromium-based catalysts

check for updates

Citation: Xing, M.; Liu, N.; Dai, C.; Chen, B. CO_2 Oxidative Dehydrogenation of Propane to Olefin over Cr-M (M = Zr, La, Fe) Based Zeolite Catalyst. *Catalysts* **2024**, *14*, 370. https://doi.org/10.3390/catal14060370

Academic Editor: Ines Graca

Received: 12 May 2024
Revised: 29 May 2024
Accepted: 4 June 2024
Published: 7 June 2024

Copyright: © 2024 by the authors. Licensee MDPI, Basel, Switzerland. This article is an open access article distributed under the terms and conditions of the Creative Commons Attribution (CC BY) license (https://creativecommons.org/licenses/by/4.0/).

1. Introduction

Low-carbon olefins, especially ethylene and propylene, can be used as basic raw materials in the synthesis of polymeric materials and fine chemicals, which play an important role in the development of the country's economy [1–4]. However, given the scarcity of oil resources and rising oil prices, the technology for producing olefins from oil needs further innovation. In recent years, the global demand for olefins has gradually increased [5]. Compared with the traditional olefin production process of cracking and splitting petroleum products, the use of low-carbon alkanes (e.g., propane) to produce olefins has the advantages of low production costs, high yields, and efficient use of resources. Olefin production from low-carbon alkanes can be divided into two types: direct alkane to olefin production, and alkane oxidation to olefin. The oxidative dehydrogenation of alkanes is an exothermic reaction that is not limited by thermodynamics [6,7]. By utilizing CO_2 as an oxidant, the conversion rate of alkane, as well as the selectivity of olefins, can be improved [4,8,9]. Moreover, it also favors the reduction of associated CO_2 emissions, which is a typical greenhouse gas that contributes to the global warming problem.

The oxidative dehydrogenation of alkanes (e.g., propane and ethane) by CO_2 (CO_2-ODHP) has been widely investigated, including through the use of Pt [10,11], Cr [12], Co [13], Ga [14,15], Mo [2,16], and B-based [17] catalysts. In comparison to other catalysts, Cr-based catalysts have the advantages of low cost and good reactivity [12]. However, problems such as carbon accumulation and easy accumulation of Cr particles occur during the catalytic reaction. The introduction of auxiliary metals into the catalyst and the selection of suitable supports to improve the dispersion of Cr species constitute two approaches to develop highly efficient Cr-based catalysts. For example, taking advantage of the large surface area and ordered pore structure of ZSM-5, with the pore size of 0.56 × 0.51 nm being larger than the molecule dynamics diameter (0.47 nm) of propane molecules, Wang et al. [18] investigated propane dehydrogenation over Cr loaded ZSM-5 (Cr-ZSM-5) zeolite, the Brönsted acid sites of which have also been reported to be favorable for the adsorption and reaction of propane. Igonina et al. [19] impregnated 5 wt.% Cr on MCM-41 using the first impregnation method, which resulted in 20% conversion of C_3H_8 and 76% selectivity of C_3H_6 at 650 °C. Singh et al. [20] used ZrO_2 as a support loaded with 2.5 wt.% Cr and achieved 16% conversion of C_3H_8 and 86.6% selectivity of C_3H_6 at 550 °C. Zhang et al. [21] introduced 5 wt.% Sn into an Al_2O_3 catalyst loaded with 3 wt.% Cr in order to improve the stability of the catalyst. The initial conversion of C_3H_8 in the catalyst was 40%, and after 10 h of reaction, the conversion of C_3H_8 was stable at 32%. Moreover, one type of composite molecular sieve of ZSM-5@SBA-15 was synthesized by adding ZSM-5 into the mother liquor of SBA-15 and was then applied for propane dehydrogenation [22,23], displaying superior catalytic activity in comparison to that of the single ZSM-5 molecular sieve.

Inspired by the above literature, a series of Cr-based ZSM-5 catalysts with different additives (Zr, La, Fe) were prepared by the impregnation method, with the aim of further improving the intrinsic CO_2-ODHP activity of Cr-ZSM-5. Additionally, in order to further improve the reaction performance, a series composite molecular sieve catalyst ($Cr_{3\%}$-ZSM-5@SBA-15 and $Cr_{3\%}Zr_{2\%}$-ZSM-5@SAB-15) was further prepared based on the hydrothermal synthesis method, in which the specific mass ratios of ZSM-5 to SBA-15 ($Cr_{3\%}$-ZS-n, n = 0.5, 2, 6, 16, representing the mass ratio) was detailed and adjusted, eventually achieving a best mass ratio of 6:1 and showing C_3H_8 conversion of 76.9% and an olefin yield of (1.72×10^3 μmol·g_{cat}^{-1}·h^{-1}) from $Cr_{3\%}Zr_{2\%}$-ZS-6. The structure–activity relationship was further illustrated by a series of characterizations (XRD, N_2 adsorption-desorption, H_2-TPR, Raman, XPS, HAAD-STEM, and TEM). The present work has developed an efficient $Cr_{3\%}Zr_{2\%}$-Z5 catalyst for the CO_2-driven oxidative dehydrogenation of propane (ODHP). Moreover, a $Cr_{3\%}Zr_{2\%}$-ZS-6 composite zeolite catalyst with promoted ODHP activity has been further developed. The present work favors the development of other highly efficient CO_2-ODHP catalyst designs.

2. Results and Discussion

2.1. Characterization of Catalysts

X-ray diffraction (XRD) was used to characterize the crystal structure of the synthesized samples. Figure 1a displays the large angle XRD characterization results of the synthesized catalyst samples. As can be seen, both the [$Cr_{3\%}$-Z5, $Cr_{3\%}M_{2\%}$-Z5 (M = La, Zr, Fe)] and composite catalyst samples ($Cr_{3\%}$-ZS-n and $Cr_{3\%}Zr_{2\%}$-ZS-6) display the characteristic MFI crystal structure at the 2θ of 8.0°, 8.9°, and 23.7° [24–26]. The loaded metal species did not significantly affect the associated crystal structure during the synthesis process, and no obvious peaks of metal oxide species, such as CrO_3 or Cr_2O_3, were observed, probably due to their good dispersion over the zeolite samples [27]. Additionally, the diffraction peaks of MFI became sharp as the mass ratio of $m_{ZSM\text{-}5}/m_{SBA\text{-}15}$ increased for the $Cr_{3\%}$-ZS-n composite. Figure 1b displays the small-angle XRD of the composite catalysts, where the characteristic diffraction patterns of SBA-15 at the 2θ of 0.8°, 1.5°, and 1.8°, corresponding to the crystalline facets of (100), (110), and (200), respectively, can be observed [27–29]. This finding indicates the successful synthesis of SBA-15. As noted, the intensity of the diffraction pattern of SBA-15 gradually decreased as the mass ratio of $m_{ZSM\text{-}5}/m_{SBA\text{-}15}$

increased. Figure 1c displays the N_2 adsorption-desorption curves of $Cr_{3\%}$-ZS-6, which displayed a typical IV curve [23], further verifying the successful synthesis of composite zeolite catalysts with mesoporous structures. The specific surface areas of the synthesized samples were characterized using the N_2 adsorption-desorption method, as listed in Table 1. The addition of the second metallic element of M (M = Zr, La, Fe) did not seriously affect the specific surface area of $Cr_{3\%}M_{2\%}$-Z5 in comparison to that of $Cr_{3\%}$-Z5 (367.7 m^2 g^{-1}). However, much higher surface areas can be achieved for the composite zeolite catalysts ($Cr_{3\%}$-ZS-n) relative to those of $Cr_{3\%}$-ZSM-5 and $Cr_{3\%}M_{2\%}$-Z5, especially for $Cr_{3\%}$-ZS-6, which showed the highest value of 505.7 m^2/g. This result indicates that encapsulation by SBA-15 can efficiently improve specific surface area, which would be favorable for the CO_2-ODHP reaction.

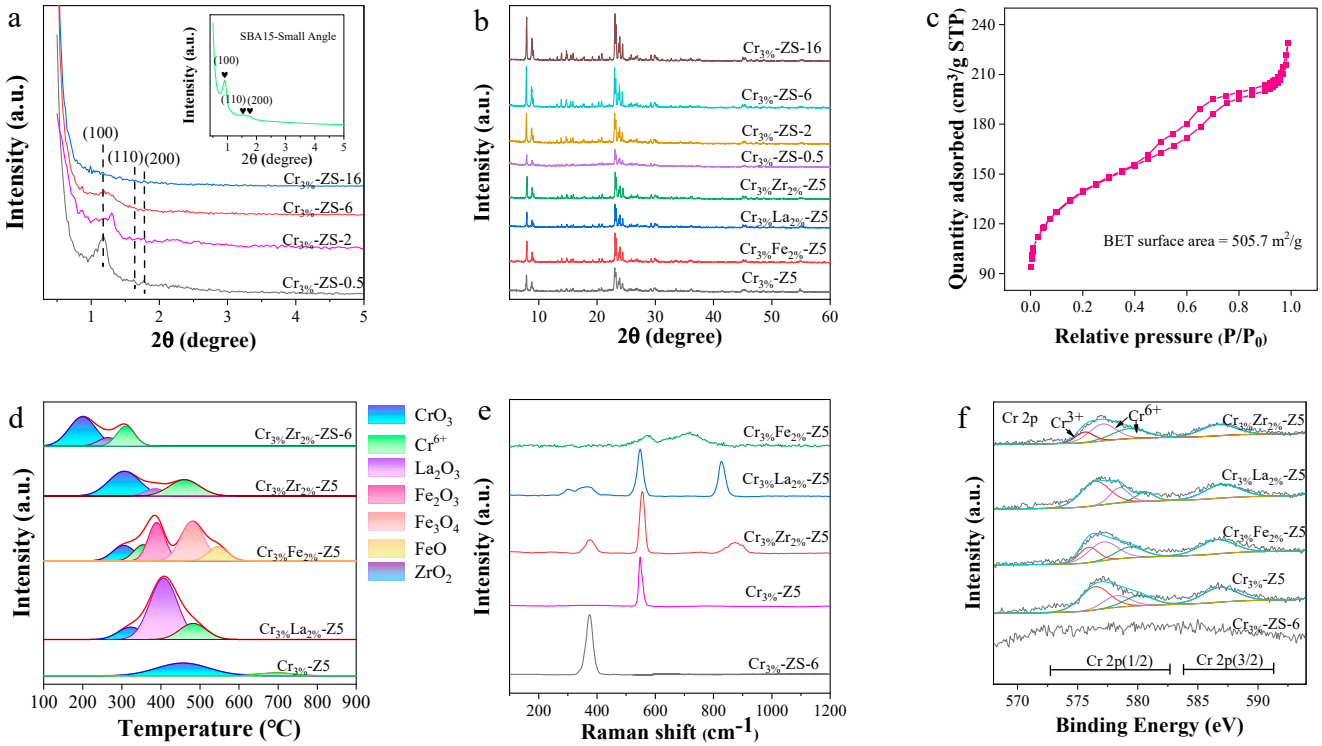

Figure 1. The characterization results of prepared Cr-based zeolite samples: (**a**) small-angle XRD, (**b**) conventional angular XRD, (**c**) N_2 physisorption-desorption isotherms of $Cr_{3\%}$-ZS-6 ($m_{ZSM\text{-}5}/m_{SBA\text{-}15}$ mass ratio of 6), (**d**) H_2-TPR (temperature-programmed reduction) profiles, (**e**) Raman spectrum, and (**f**) XPS spectra. As noted, the ZSM-5 was abbreviated as Z5, and the ZSM-5@SBA-15 was abbreviated as ZS.

Table 1. Specific surface area and Cr^{6+} ratio of the prepared Cr-based zeolite catalysts.

Sample	S_{BET} [a], m^2/g	$Cr^{6+}/(Cr^{6+} + Cr^{3+})$
$Cr_{3\%}$-Z5	367.7	46.9%
$Cr_{3\%}Zr_{2\%}$-Z5	324.2	71.1%
$Cr_{3\%}La_{2\%}$-Z5	363.2	68.2%
$Cr_{3\%}Fe_{2\%}$-Z5	376.2	73.9%
$Cr_{3\%}$-ZS-0.5	456.2	—
$Cr_{3\%}$-ZS-2	469.8	—
$Cr_{3\%}$-ZS-6	505.7	—
$Cr_{3\%}$-ZS-16	403.0	—

[a] S_{BET}: BET specific surface area.

H_2-TPR was conducted to characterize the specific chemical states of the loaded Cr and M (Zr, La, Fe) species over the synthesized catalyst samples (see Figure 1d). For $Cr_{3\%}$-Z5, the broad peak centered at *T* of 300–400 °C can be attributed to the reduction of CrO_3 species, and the weak reduction peak at *T* of 400–500 °C can be attributed to the reduction of Cr^{6+} [30,31]. As for the $Cr_{3\%}M_{2\%}$-Z5 samples, in addition to the abovementioned reduction peaks of CrO_3 and Cr^{6+}, the additional reduction peaks of the (Zr, La, Fe) species could also be clearly identified. Specifically, for the $Cr_{3\%}Fe_{2\%}$-ZSM-5 sample, the reduction peak around 400 °C was related to the reduction of Fe_2O_3 to Fe_3O_4; the peak around 500 °C was attributed to the reduction of Fe_3O_4 to FeO; and the peak around 600 °C was ascribed to the reduction of FeO to Fe [32]. As for $Cr_{3\%}Zr_{2\%}$-Z5 and $Cr_{3\%}La_{2\%}$-Z5, the additional reduction peaks at *T* of 300–400 °C and 400–500 °C were related to the reductions of ZrO_2 and La_2O_3, respectively [33,34]. As noted above, after the introduction of Zr, the reduction peaks of Cr ($CrO_3 \rightarrow Cr_2O_3$) were shifted to lower temperatures (450 → 290 °C), and also developed a larger reduction peak area. This was closely related to the fact that ZrO_2, which is a P-type semiconductor, formed a strong interaction with the active metal Cr, favoring the reduction of CrO_3, which is conducive to CO_2-ODHP. Similarly, in the $Cr_{3\%}La_{2\%}$-Z5 and $Cr_{3\%}Fe_{2\%}$-Z5 scenarios, it is evident that the presence of La and Fe additives also promoted the reduction of CrO_3 to Cr_2O_3, although to a lesser extent compared to Zr. This constitutes one of the major reasons leading to the lower CO_2-ODOH activity of $Cr_{3\%}Zr_{2\%}$-Z5 than that observed for $Cr_{3\%}La_{2\%}$-Z5 and $Cr_{3\%}Fe_{2\%}$-Z5 (as will be stated later). In addition to this, for the composite zeolite catalyst $Cr_{3\%}Zr_{2\%}$-ZS-6, it was found that, interestingly, the reduction peaks of CrO_3 and Cr^{6+} further shifted to lower temperatures (450 → 200 °C) due to encapsulation by SBA-15. This favored the dispersion of the Cr species. This is also one of the main reasons for the further improvement in the CO_2-ODH activity in this sample compared to that of $Cr_{3\%}Zr_{2\%}$-Z5.

Raman spectroscopy was further used to characterize the loaded Cr species over the synthesized samples, as shown in Figure 1e, where the peak centered at 550 cm^{-1} can be attributed to the Cr-O vibration of Cr_2O_3 species over $Cr_{3\%}$-Z5. In addition to the peak at 550 cm^{-1}, the Raman peaks corresponding to $Cr_2O_7^{2-}$ (350–400 cm^{-1} of $Cr_{3\%}Zr_{2\%}$-Z5), $Cr_3O_{10}^{2-}$ (850 cm^{-1} of $Cr_{3\%}La_{2\%}$-Z5) and $Cr_4O_{13}^{2-}$ (900 cm^{-1} of $Cr_{3\%}Zr_{2\%}$-Z5) appeared after the introduction of Zr and La [35]. Only one Raman peak of $Cr_2O_7^{2-}$ (350–400 cm^{-1}) emerged over the composite $Cr_{3\%}$-ZS-6. The above results indicate that the addition of the second metal, as well as encapsulation by SBA-15 (generating composite catalyst), could significantly affect the valence state of CrO_x. According to a previous report in the literature [36], the formed $Cr_2O_7^{2-}$ and $Cr_4O_{13}^{2-}$ species would be more active for the ODHP reaction relative to that of Cr_2O_3. Thus, the results there (Figure 1) give a further indication of the much higher CO_2-ODHP of $Cr_{3\%}Zr_{2\%}$-Z5 and $Cr_{3\%}$-ZS-6 relative to that of $Cr_{3\%}$-Z5. As noted above, no characteristic Raman peaks of CrO_x species could be found over $Cr_{3\%}Fe_{2\%}$-Z5, which was probably related to the tendency of FeO_x to react with oxygen in air to form an oxide film, which eventually interferes with Raman spectroscopic analysis.

The valence states of the active metal Cr over the synthesized samples were further analyzed by XPS (Figure 1f), with the derived $Cr^{6+}/(Cr^{6+}+Cr^{3+})$ ratios being listed in Table 1. As can be seen, the Cr 2p1/2 for the investigated samples could be split into three peaks, of which the characteristic peaks with electron binding energies at 575.0 eV were attributed to Cr^{3+}, and the two other peaks with electron binding energies of 577.2 and 579.0 eV were attributed to Cr^{6+} [37]. As listed in Table 1, the $Cr^{6+}/(Cr^{6+}+Cr^{3+})$ ratios of bimetallic modified ZSM-5 samples (68.2–73.9%) were much higher than that of monometallic $Cr_{3\%}$/ZSM-5 (46.9%), indicating that the second metal additives favored the formation of Cr^{6+} species, which have much higher activity than that of Cr^{3+}. In this regard, the addition of the second metal promoted the Cr^{6+} ratio relative to the single-metal-promoted $Cr_{3\%}$-Z5, which is another important reason leading to the much higher CO_2-ODHP activity. As noted, no XPS signal of Cr species was observed over $Cr_{3\%}$-ZS-6, which could be related to the encapsulation of $Cr_{3\%}$-ZSM-5 by SBA-15, leading to the Cr being undetectable.

Figure 2 shows the HAADF-STEM, HRTEM, and EDS-mapping results of $Cr_{3\%}$-Z5 (Figure 2a–c), $Cr_{3\%}Zr_{2\%}$-Z5 (Figure 2d–f) and $Cr_{3\%}Zr_{2\%}$-ZS-6 (Figure 2g–i), which provide information on the crystalline structure and surface distribution of the active metal Cr. As compared in Figure 2a,d,g, the Cr agglomerates can be clearly observed over $Cr_{3\%}$-Z5; however, they cannot be seen over the samples of $Cr_{3\%}Zr_{2\%}$-Z5 and $Cr_{3\%}Zr_{2\%}$-ZS-6. This finding is well supported by the EDS-mapping results shown in Figure 2c,f,i, displaying the aggregated Cr nanoparticles over $Cr_{3\%}$-Z5 and the monodispersed Cr over $Cr_{3\%}Zr_{2\%}$-Z5 and $Cr_{3\%}Zr_{2\%}$-ZS-6. This finding gives us a clue that the addition of Zr (Figure S1), as well as encapsulation by SBA-15, could favor the dispersion of loaded Cr species. In addition, the obvious lattice stripes at 0.375 nm belonging to the (151) plane of ZSM-5 [38] can be clearly observed for the investigated samples (Figure 2b,e,h), and the regular pore structure of SBA-15 [29], with a clear interface between SBA-15 and ZSM-5, can also be observed in Figure 2h, verifying the successful synthesis of the $Cr_{3\%}Zr_{2\%}$-ZS-6 composite.

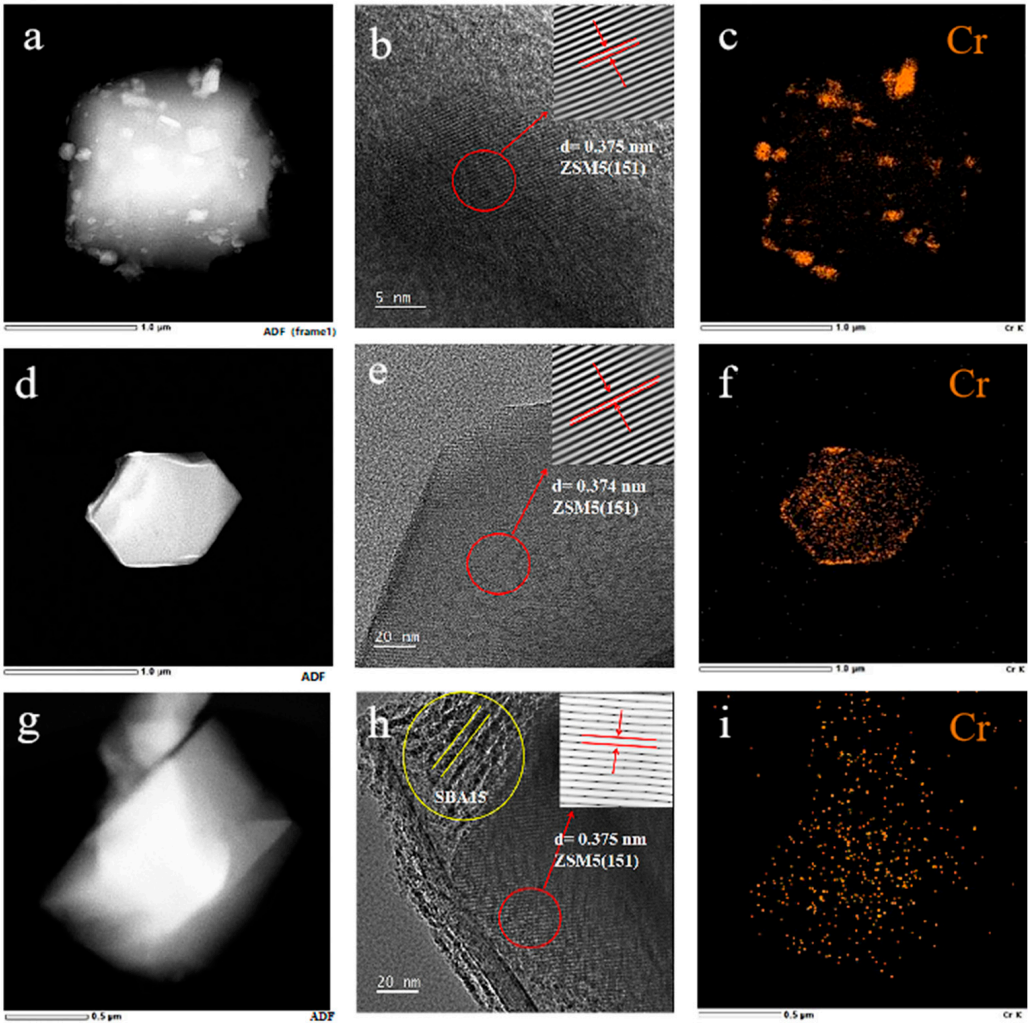

Figure 2. HAADF-STEM, HRTEM, and EDS-mapping images of (**a**–**c**) $Cr_{3\%}$-Z5, (**d**–**f**) $Cr_{3\%}Zr_{2\%}$-Z5, and (**g**–**i**) $Cr_{3\%}Zr_{2\%}$-ZS-6.

2.2. Reaction Mechanism Investigation

In situ FTIR was employed to investigate the CO_2-ODHP reaction mechanism over the best-performing sample of $Cr_{3\%}Zr_{2\%}$-ZS-6 at *T* of 250–500 °C, as shown in Figure 3. Several intermediate species with IR vibration peaks centered at 1700–1350 cm^{-1} were identified, including the methyl radical [CH_3*] in the range of 1400–1370 cm^{-1} [34], polydentate carbonate species around 1468 cm^{-1} [39], H_2O around 1640 cm^{-1}, and olefins with the telescopic vibrational peak of C=C around 1650 cm^{-1} [40]. As noted, the other peaks in the

range of 3600–3750 cm^{-1} belonged to hydroxyl species [OH*], and the 1501 cm^{-1} peak was attributed to be the telescopic vibrational peak of the Brönsted acid site [41]. Based on the above derived intermediate information, as well as reports from the literature [36], it can be proposed that CO_2-ODHP would follow the Mars–van Krevelen mechanism [42]. First, CO_2 is adsorbed on the support at a low temperature (T of 250 °C), forming polydentate carbonates (1468 cm^{-1}). The reaction from propane to olefin then begins with an increase in temperature (T > 300 °C), where the polydentate carbonates participate in the reaction with a gradual decrease in the IR signal (1470 cm^{-1}) and a simultaneous gradual increase in the IR signal of olefin ($\upsilon_{C=C}$ of 1649 cm^{-1}) and H_2O (υ_{H2O} of 1625 cm^{-1}). As reported [43], Cr^{6+} is the activation site for the propane dehydrogenation reaction, and the C-H bond broken to produce radicals of C_3H_7* (1370–1400 cm^{-1}, Figure 3) and H* is reported to be the rate-determining step (RDS). In addition to C_3H_6, C_2H_4 and CH_4 were also observed during activity measurement. This can be attributed to the strong C-C bond breaking effect of the Brönsted acid site (around 1540 cm^{-1}) of the ZSM-5 support. The interaction of C_3H_8 with a Brönsted acid site leads to the breaking of the C-C bond, generating radicals of ethyl (C_2H_5*) and (CH_3*) methyl (1400–1370 cm^{-1}, Figure 3). Subsequently, the broken C-H bond of C_2H_5* leads to the formation of C_2H_4 and the dissociated proton H*, which further interacts with the radical of CH_3* to produce CH_4. Based on the above discussion, we can conclude that the Cr^{6+} is the activation site for propane dehydrogenation, where CO_2 participates in the reaction as polydentate carbonates. Assisted by the Brönsted acid site (favoring C-C bond breaking), C_2H_4 and CH_4 are produced. As noted, after the dehydrogenation reaction, Cr^{6+} is reduced to Cr^{3+}, which is then further oxidized to Cr^{6+} by CO_2, forming polydentate carbonates and thus cycling the reactive species Cr^{6+}. The CO_2/C_3H_8 adsorption over ZrO2 [111] and CrO3 [110] was further simulated by DFT to further illustrate the role played by Zr during CO_2-ODHP. The results are shown in Tables S1 and S2. As can be seen, the adsorption energies of CO_2 and C_3H_8 on the ZrO_2 were −0.14 eV and −0.03 eV, and those of CrO_3 were −0.09 and −0.06 eV, respectively. Obviously, the ZrO_2 exhibited a much lower CO_2 adsorption energy (−0.14 eV) than that of CrO_3 (−0.09 eV). This finding indicates that the introduced Zr also functioned as the active site during CO_2-ODHP, favoring CO_2 adsorption over the Cr-based ZSM-5 zeolite.

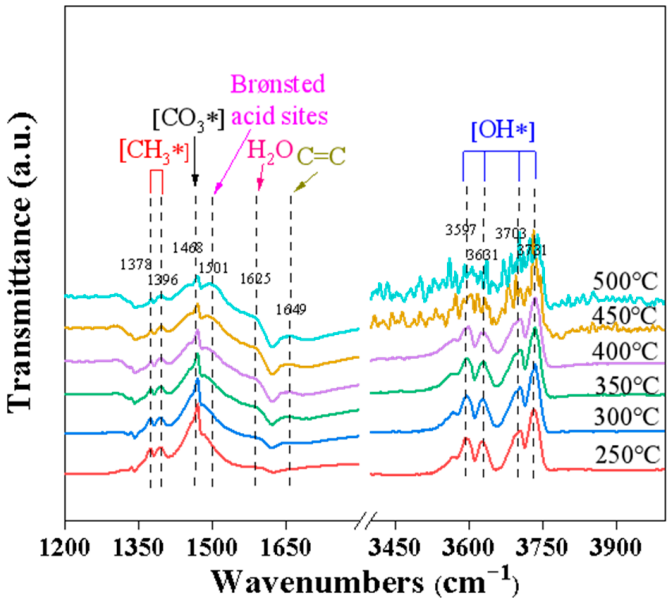

Figure 3. In situ FTIR over $Cr_{3\%}Zr_{2\%}$-ZS-6. Reaction conditions: the sample was first pretreated at 500 °C under an H_2 atmosphere for 1 h. Then, the temperature was lowered to room temperature, followed by the simultaneous introduction of a mixed gas comprising 5% C_3H_8 and 5% CO_2, balanced by He (total flow rate of 20 mL/min) and introduced into the sample under 250, 300, 350, 400, 450, and 500 °C for 30 min.

2.3. Catalytic Activity of Cr-Based Catalysts

Figure 4a,b display the propane conversion, CO_2 conversion, olefin selectivity, and olefin yield of the synthesized samples of $Cr_{3\%}M_{2\%}$-Z5 (M = Zr, La, Fe), where the Cr loading was 3 wt.% and the additive metal loading was 2 wt.%. The proportion of each product (C_3H_6, C_2H_4, C_2H_6, CH_4) is depicted in Figure S2a. As can be seen, adding additional metals, such as Zr, La, and Fe, increased C_3H_8 conversion and olefin yield; this was accompanied by a slight decrease in olefin selectivity (62.9 → 58.6%). Among the samples, $Cr_{3\%}Zr_{2\%}$-Z5 displayed the best CO_2-ODHP catalytic behavior, achieving C_3H_8 conversion of 65.4% and an olefin yield of 1.65 × 10^3 μmol·g_{cat}^{-1}·h^{-1}. Figure 4c,d display the activity measurement results for the composite catalysts of $Cr_{3\%}$-ZS-n (n = 0.5, 2, 6, 16) and $Cr_{3\%}Zr_{2\%}$-ZS-6, wherein the ZSM-5: SBA-15 ratio of 6:1 led to much higher C_3H_8 conversion (73.7%) and olefin yield (1.69 × 10^3 μmol·g_{cat}^{-1}·h^{-1}) than those of the other catalysts. The distribution of each element (C_3H_6, C_2H_4, C_2H_6, CH_4) in the product is shown in Figure S2b, showing a slight decrease in olefin selectivity up to 52.0%. Moreover, the C_3H_8 conversion and olefin yield was further improved to 76.9% and 1.72 × 10^3 μmol·g_{cat}^{-1}·h^{-1}, respectively, over the bimetallic composite molecular sieve of $Cr_{3\%}Zr_{2\%}$-ZS-6 (mass ratio of 6.0) due to the superior intrinsic CO_2-ODHP activity of $Cr_{3\%}Zr_{2\%}$-Z5 compared to that of $Cr_{3\%}$-Z5 (Figure 4a,b). It can be seen from Figure S3 that the activity of the catalysts ($Cr_{3\%}$-Z5, $Cr_{3\%}Zr_{2\%}$-Z5, and $Cr_{3\%}Zr_{2\%}$-ZS-6) decreased slightly after 180 min of reaction time.

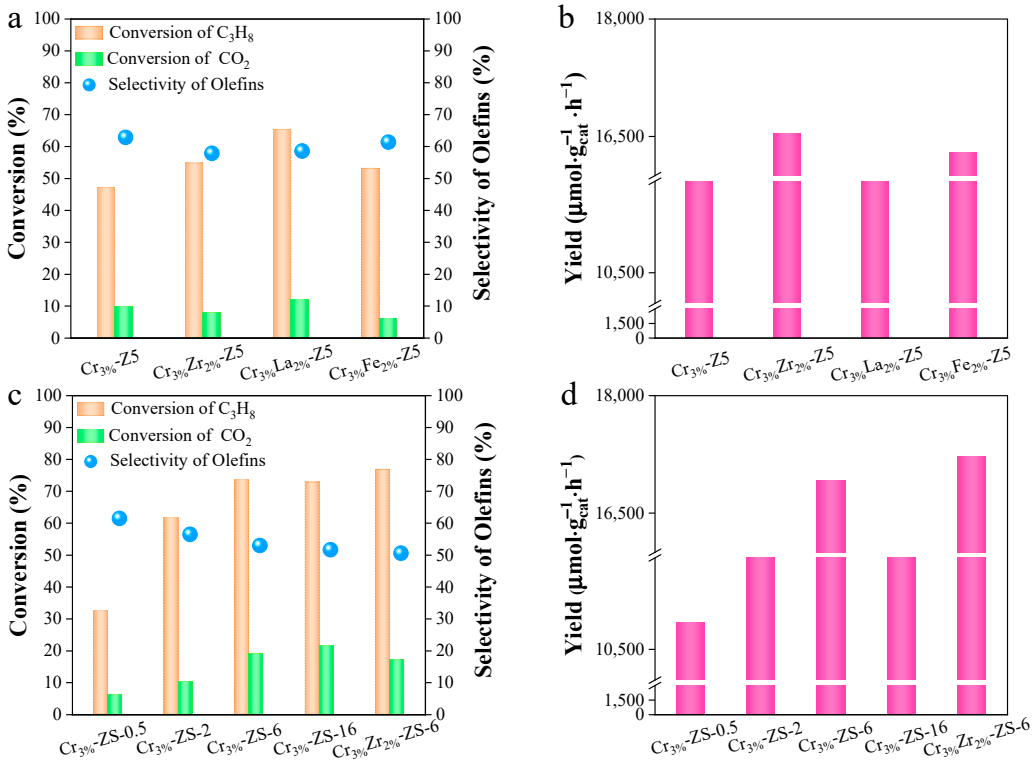

Figure 4. Catalytic performance evaluation of the synthesized samples of (**a**,**b**) $Cr_{3\%}$-Z5, $Cr_{3\%}M_{2\%}$-Z5 (M = La, Zr, Fe) and (**c**,**d**) $Cr_{3\%}$-ZS-n (n = 0.5, 2, 6, 16) as well as $Cr_{3\%}Zr_{2\%}$-ZS-6 (mass ratio of 6), including propane and CO_2 conversion and olefin selectivity and yield. Reduction conditions: T = 600 °C, GHSV = 12,000 h^{-1}, C_3H_8:CO_2:He = 2:2:16. As noted, ZSM-5 was abbreviated as Z5, and ZSM-5@SBA-15 was abbreviated as ZS.

3. Material and Methods

3.1. Preparation of Cr-Based ZSM-5 Zeolite Catalyst

Approximately 0.476 g of $Cr(NO_3)_3·9H_2O$ and a certain amount of nitrate compounds of the additive metals were weighed into a 250 mL tomato-shaped bottle. Then, 50 mL of deionized water and 2 g of ZSM-5 carrier with an Si:Al ratio of 50 were added and stirred

in a water bath at 90 °C for 4 h. The tomato-shaped bottle containing the sample was mounted on a spinner to remove water, and was thereafter placed in an oven at 60 °C and dried overnight. Finally, the sample was calcined in a muffle furnace at 550 °C under air atmosphere for 6 h to obtain the $Cr_{3\%}$-Z5 and $Cr_{3\%}M_{2\%}$-Z5 (M = Zr, La, Fe) samples.

3.2. Preparation of Cr-Based ZSM-5@SBA-15 Composite Zeolite Catalyst

SBA-15 was prepared by using triblock copolymer P123 as the structure-directing agent and tetraethyl silicate TEOs as the silicon source. First, 0.326 g of P123 was dissolved in 50 mL of 1.6 mol/L hydrochloric acid and stirred for 15 min in a water bath at 40 °C. Then, 0.75 mL of tetraethyl silicate was added and stirred continuously for 40 min to form the mother solution of SBA-15. A certain amount of $Cr(NO_3)_3 \cdot 9H_2O$ and ZSM-5 molecular sieves (Si:Al = 50) were added to the mother solution of SBA-15 according to the mass ratios of ZSM-5 to SBA-15 of 0.5, 2, 6, and 16, respectively, and stirred for 24 h. After that, the samples were placed in a crystallization tank at 100 °C for 24 h. Then, after washing three times with water and alcohol, centrifugation, drying (60 °C for 12 h), and calcination (550 °C for 6 h), the $Cr_{3\%}$-ZS-n (n = 0.5, 2, 6, 16) was obtained. A similar procedure was also applied during $Cr_{3\%}Zr_{2\%}$-ZS-6 preparation, utilizing $Zr(NO_3)_3 \cdot 5H_2O$ as the Zr precursor.

3.3. Characterizations

X-ray diffraction (XRD) was performed on a D8 Advance instrument (Karlsruhe, Germany) to analyze the crystalline phase structure of the catalyst samples using a Cu Kα radiation source in the range of 5–60°. Specific surface area analysis (BET) was carried out on an Autosorb iQ (Boynton Beach, FL, USA) adsorption apparatus to analyze the specific surface area of the catalyst samples, and N_2 adsorption and desorption curves were obtained using an Autosorb iQ adsorption apparatus. The samples were degassed at 300 °C for 6 h. H_2 programmed temperature rising reduction (H_2-TPR) was carried out on a fully automated multicurrent apparatus, the tp-5080-B (Tianjin, Beijing), and was used to analyze the composition of the metal oxide species of the samples. A 0.1 g sample was first pretreated at 100 °C for 10 min, then cooled to room temperature to level the baseline, and finally heated from 100 to 900 °C at a rate of 10 °C/min. Raman spectroscopy (Raman) was performed on a LabRam HR Evolution Raman spectrometer (Paris, France) in the range of 100 to 1200 cm^{-1} with a laser wavelength of 532 nm. X-ray photoelectron spectroscopy (XPS) was performed on a Thermo Scientific K-Alpha X-ray photoelectron spectrometer, Waltham, MA, USA, to analyze the material composition of the samples. Transmission electron microscopy (TEM) was performed using a JEOL JEM-F200 transmission electron microscope (Tokyo, Japan) to observe the structural compositions of the catalyst samples, which were first sonicated in ethanol for 60 min and then added drop-wise to a copper grid to prepare the samples for measurement. In situ Fourier infrared spectroscopy (FTIR) was carried out using a BRUKER (Billerica, MA, USA) TENSOR II infrared spectrometer and was used to measure the functional groups and chemical compositions etc. produced during the reaction. Infrared variable temperature experiments were conducted, in which the samples to be measured were pressed and first pretreated with H_2 at 500 °C for 60 min, before being cooled to room temperature. Then, a mixed gas comprising 5% C_3H_8 and 5% CO_2, balanced by He (total flow rate of 20 mL/min), was introduced into the sample under temperatures of 250, 300, 350, 400, 450, and 500 °C for 30 min, with the IR signal being collected each minute.

3.4. Catalytic Test

The CO_2-ODHP activity measurement was carried out in a continuous flow fixed bed reactor under atmospheric pressure and *T* of 600 °C. The volume ratio of the feed gas was set to be C_3H_8:CO_2:He = 2:2:16. The gas hourly velocity (GHSV) was 12,000 h^{-1}. As noted, before the reaction, 0.1 g of catalyst (40–60 mesh) was initially pretreated using 5% H_2 in He for 60 min at 600 °C. The composition of the reacted gas, as well as the product, were analyzed on-line using an SP-7890 gas chromatograph with a TCD detector (Shimadzu,

Kyoto, Japan). The propane conversion, CO_2 conversion, olefin selectivity, and olefin yield were calculated by Equations (1)–(4), as shown below:

$$X_{C_3H_8} = \frac{C_3H_8(in) - C_3H_8(out)}{C_3H_8(in)} \times 100\% \quad (1)$$

$$X_{CO_2} = \frac{CO_2(in) - CO_2(out)}{CO_2(in)} \times 100\% \quad (2)$$

$$S_{olefins} = \frac{3C_3H_6 + 2C_2H_4}{3C_3H_6 + 2C_2H_6 + 2C_2H_4 + CH_4} \times 100\% \quad (3)$$

$$\text{Yield of olefins} = \frac{\Delta PPm \times Fin \times 60 \times 273 \times 10^4}{T \times M_{cat} \times 22.4 \times 10^3} \quad (4)$$

where F_{in} represents the flow rate of gases introduced (C_3H_8 and CO_2); ΔPPm represents the increase in propylene and ethylene; T represents reaction temperature; and M_{cat} represents the mass of catalyst.

4. Conclusions

In conclusion, a series of Cr-based zeolite catalysts were prepared for CO_2-ODHP with the aim of providing a type of candidate catalyst that not only favors propane conversion to olefin, but also contributes to CO_2 emission control. It was found that the addition of a second metal (Zr, La, or Fe) enhanced CO_2-ODHP activity relative to that of single metal Cr promoted ZSM-5 ($Cr_{3\%}$-Z5), with Zr exhibiting the most pronounced effect. Characterizations using H_2-TPR, XPS, Raman spectroscopy, and HAAD-STEM suggested that the addition of Zr improved the redox ability of Cr, increased the Cr^{6+} species ratio (which acted as active sites for the reaction), and favored the dispersion of Cr species over the ZSM-5 support, which together constituted three major factors leading to the superior CO_2-ODHP activity of $Cr_{3\%}Zr_{2\%}$-Z5. In addition, one zeolite composite, in which $Cr_{3\%}Zr_{2\%}$-Z5 was encapsulated by SBA-15 ($m_{Cr3\%\text{-}ZSM\text{-}5}/m_{SBA\text{-}15}$ mass ratio of 6), was prepared using the hydrothermal synthesis method, which further promoted CO_2-ODHP activity due to the large surface area of SBA-15 favoring the dispersion of active Cr species. Finally, the CO_2-ODHP reaction mechanism was investigated using in situ FTIR. It was found that the reaction followed the Mars–van Krevelen mechanism, wherein the CO_2 was initially adsorbed over the $Cr_{3\%}Zr_{2\%}$-ZS-6, forming polydentate carbonates, nand then participated in the reaction through reacting with dissociated H* from C_3H_8 to produce H_2O and C_3H_6. Additionally, assisted by the Brönsted acid site (favoring C-C bond breaking), C_2H_4 and CH_4 were generated. In general, the present work investigated CO_2-ODHP over a series of Cr-based zeolite catalysts, based on which one $Cr_{3\%}Zr_{2\%}$-ZS-6 candidate composite catalyst was screened out. The present work favors the development of CO_2-ODHP techniques.

Supplementary Materials: The following supporting information can be downloaded at: https://www.mdpi.com/article/10.3390/catal14060370/s1, Figure S1. EDS-Mapping image of Zr in catalyst $Cr_{3\%}Zr_{2\%}$-Z5. Figure S2. Selectivity of the synthesized samples of (a) $Cr_{3\%}$-Z5, $Cr_{3\%}M_{2\%}$-Z5 (M = La, Zr, Fe) and (b) $Cr_{3\%}$-ZS-n (n = 0.5, 2, 6, 16) as well as $Cr_{3\%}Zr_{2\%}$-ZS-6 (mass ratio of 6). Figure S3. Conversion of propane with catalysts $Cr_{3\%}$-Z5, $Cr_{3\%}Zr_{2\%}$-Z5 and $Cr_{3\%}Zr_{2\%}$-ZS-6 (reaction time: 180 min). Table S1. Model diagram of CO_2 and C_3H_8 adsorption over CrO3 [110] and ZrO2 [111]. Table S2. Adsorption energy of CO_2 and C_3H_8 over CrO3 [110] and ZrO2 [111]. Ref. [44] is cited in Supplementary Materials.

Author Contributions: Conceptualization, B.C. and N.L.; methodology, M.X.; validation, C.D. and M.X.; resources, B.C. and N.L.; writing, original draft preparation, M.X.; writing, review and editing, N.L.; supervision, B.C. and N.L.; project administration, B.C. and N.L. All authors have read and agreed to the published version of the manuscript.

Funding: This research was funded by National Natural Science Foundation of China (No. 22178011, 22176006).

Data Availability Statement: Data are contained within the article and Supplementary Materials.

Conflicts of Interest: The authors declare no competing interests.

References

1. Atanga, M.A.; Rezaei, F.; Jawad, A.; Fitch, M.; Rownaghi, A.A. Oxidative dehydrogenation of propane to propylene with carbon dioxide. *Appl. Catal. B Environ.* **2018**, *220*, 429–445. [CrossRef]
2. Bagheri, S.; Julkapli, N.M. Mo_3VO_x catalyst in biomass conversion: A review in structural evolution and reaction pathways. *Int. J. Hydrogen Energy.* **2017**, *42*, 2116–2126. [CrossRef]
3. Li, C.; Wang, G. Dehydrogenation of light alkanes to mono-olefins. *Chem. Soc. Rev.* **2021**, *50*, 4359–4381. [CrossRef]
4. Yuan, Y.; Porter, W.N.; Chen, J.G. Comparison of direct and CO_2-oxidative dehydrogenation of propane. *Trends. Chem.* **2023**, *5*, 840–852. [CrossRef]
5. Shou, H.; Dasari, P.R.; Broekhuis, R.R.; Mondal, A.; Patel, A.; Nguyen, C.; Fickel, D.W. Cracking of Butane on a Pt/H-ZSM-5 Catalyst in the Presence of Hydrogen. *Ind. Eng. Chem. Res.* **2022**, *61*, 4763–4773. [CrossRef]
6. Hu, Z.-P.; Yang, D.; Wang, Z.; Yuan, Z.-Y. State-of-the-art catalysts for direct dehydrogenation of propane to propylene. *Chin. J. Catal.* **2019**, *40*, 1233–1254. [CrossRef]
7. Qu, Y.; Li, G.; Zhao, T.; Zhang, Z.; Douthwaite, M.; Zhang, J.; Hao, Z. Low-temperature direct dehydrogenation of propane over binary oxide catalysts: Insights into geometric effects and active sites. *ACS Sustain. Chem. Eng.* **2021**, *9*, 12755–12765. [CrossRef]
8. Mukherjee, D.; Park, S.-E.; Reddy, B.M. CO_2 as a soft oxidant for oxidative dehydrogenation reaction: An eco benign process for industry. *J. CO_2 Util.* **2016**, *16*, 301–312. [CrossRef]
9. Otroshchenko, T.; Jiang, G.; Kondratenko, V.A.; Rodemerck, U.; Kondratenko, E.V. Current status and perspectives in oxidative, non-oxidative and CO_2-mediated dehydrogenation of propane and isobutane over metal oxide catalysts. *Chem. Soc. Rev.* **2021**, *50*, 473–527. [CrossRef]
10. Lian, Z.; Si, C.; Jan, F.; Zhi, S.; Li, B. Coke deposition on Pt-based catalysts in propane direct dehydrogenation: Kinetics, suppression, andl eimination. *ACS Catal.* **2021**, *11*, 9279–9292. [CrossRef]
11. Zhu, J.; Wang, T.; Xu, X.; Xiao, P.; Li, J. Pt nanoparticles supported on SBA-15: Synthesis, characterization and applications in heterogeneous catalysis. *Appl. Catal. B Environ.* **2013**, *130*, 197–217. [CrossRef]
12. Dai, Y.; Gao, X.; Wang, Q.; Wan, X.; Zhou, C.; Yang, Y. Recent progress in heterogeneous metal and metal oxide catalysts for direct dehydrogenation of ethane and propane. *Chem. Soc. Rev.* **2021**, *50*, 5590–5630. [CrossRef] [PubMed]
13. Barsan, M.M.; Thyrion, F.C. Kinetic study of oxidative dehydrogenation of propane over Ni-Co molybdate catalyst. *Catal. Today* **2003**, *81*, 159–170. [CrossRef]
14. Liu, D.; Cao, L.; Zhang, G.; Zhao, L.; Gao, J.; Xu, C. Catalytic conversion of light alkanes to aromatics by metal-containing HZSM-5 zeolite catalysts-A review. *Fuel Process. Technol.* **2021**, *216*, 106770. [CrossRef]
15. Yuan, Y.; Zhao, Z.; Lobo, R.F.; Xu, B. Site diversity and mechanism of metal-exchanged zeolite catalyzed non-oxidative propane dehydrogenation. *Adv. Sci.* **2023**, *10*, 2207756. [CrossRef] [PubMed]
16. Madeira, L.M.; Portela, M.F.; Mazzocchia, C. Nickel molybdate catalysts and their use in the selective oxidation of hydrocarbons. *Catal. Rev. Sci. Eng.* **2004**, *46*, 53–110. [CrossRef]
17. Love, A.M.; Cendejas, M.C.; Thomas, B.; McDermott, W.P.; Uchupalanun, P.; Kruszynski, C.; Burt, S.P.; Agbi, T.; Rossini, A.J.; Hermans, I. Synthesis and characterization of silica-supported boron oxide catalysts for the oxidative dehydrogenation of propane. *J. Phys. Chem. C* **2019**, *123*, 27000–27011. [CrossRef]
18. Silva, B.; Figueiredo, H.; Soares, O.S.G.P.; Pereira, M.F.R.; Figueiredo, J.L.; Lewandowska, A.E.; Banares, M.A.; Neves, I.C.; Tavares, T. Evaluation of ion exchange-modified Y and ZSM5 zeolites in Cr(VI) biosorption and catalytic oxidation of ethyl acetate. *Appl. Catal. B Environ.* **2012**, *117*, 406–413. [CrossRef]
19. Igonina, M.; Tedeeva, M.; Kalmykov, K.; Kapustin, G.; Nissenbaum, V.; Mishin, I.; Pribytkov, P.; Dunaev, S.; Kustov, L.; Kustov, A. Properties of CrO_x/MCM-41 and its catalytic activity in the reaction of propane dehydrogenation in the presence of CO_2. *Catalysts* **2023**, *13*, 906. [CrossRef]
20. Singh, R.; Nayak, S.C.; Singh, R.; Deo, G. O_2 and CO_2 assisted oxidative dehydrogenation of propane using ZrO_2 supported vanadium and chromium oxide catalysts. *Catal. Today* **2024**, *432*, 114617. [CrossRef]
21. Zhang, L.; Chen, K.; Chen, H.; Han, X.; Liu, C.; Qiao, L.; Wu, W.; Yang, B. Elucidating the promoting advantages and fundamentals for their creation in Sn-modified commercial CrO_x/Al_2O_3 catalyst for propane dehydrogenation. *Chem. Eng. J.* **2024**, *483*, 149366. [CrossRef]
22. Razavian, M.; Fatemi, S. Synthesis and application of ZSM-5/SAPO-34 and SAPO-34/ZSM-5 composite systems for propylene yield enhancement in propane dehydrogenation process. *Micropor. Mesopor. Mat.* **2015**, *201*, 176–189. [CrossRef]
23. Zhang, L.; Zhao, Y.; Dai, H.; He, H.; Au, C.T. A comparative investigation on the properties of Cr-SBA-15 and CrO_x/SBA-15. *Catal. Today* **2008**, *131*, 42–54. [CrossRef]
24. Ji, F.; Li, C.; Liu, Y.; Liu, P. Heterogeneous activation of peroxymonosulfate by Cu/ZSM5 for decolorization of Rhodamine B. *Sep. Purif. Technol.* **2014**, *135*, 1–6. [CrossRef]

25. Kim, M.-S.; Lee, D.-W.; Chung, S.-H.; Hong, Y.-K.; Lee, S.H.; Oh, S.-H.; Cho, I.-H.; Lee, K.-Y. Oxidation of ammonia to nitrogen over Pt/Fe/ZSM5 catalyst: Influence of catalyst support on the low temperature activity. *J. Hazard. Mater.* **2012**, *237*, 153–160. [CrossRef] [PubMed]
26. Saba, T.; Estephane, J.; El Khoury, B.; El Khoury, M.; Khazma, M.; El Zakhem, H.; Aouad, S. Biodiesel production from refined sunflower vegetable oil over KOH/ZSM5 catalysts. *Renew. Energy* **2016**, *90*, 301–306. [CrossRef]
27. Tian, J.; Guan, J.; Xu, M.; Qian, S.; Ma, K.; Wan, S.; Zhang, Z.; Xiong, H.; Wang, S.; Wang, Y.; et al. Repairing vacancy defects for stabilization of high surface area hexagonal boron nitride under harsh conditions. *Chem. Eng. J.* **2023**, *475*, 146015. [CrossRef]
28. Aboul-Enein, A.A.; Soliman, F.S.; Betiha, M.A. Co-production of hydrogen and carbon nanomaterials using NiCu/SBA15 catalysts by pyrolysis of a wax by-product: Effect of Ni-Cu loading on the catalytic activity. *Int. J. Hydrogen Energy* **2019**, *44*, 31104–31120. [CrossRef]
29. Yang, W.; Liu, H.; Li, Y.; Wu, H.; He, D. CO_2 reforming of methane to syngas over highly-stable Ni/SBA-15 catalysts prepared by P123-assisted method. *Int. J. Hydrogen Energy* **2016**, *41*, 1513–1523. [CrossRef]
30. Al-Awadi, A.S.; El-Toni, A.M.; Al-Zahrani, S.M.; Abasaeed, A.E.; Alhoshan, M.; Khan, A.; Labis, J.P.; Al-Fatesh, A. Role of TiO_2 nanoparticle modification of Cr/MCM41 catalyst to enhance Cr-support interaction for oxidative dehydrogenation of ethane with carbon dioxide. *Appl. Catal. A Gen.* **2019**, *584*, 117114.
31. Zhang, Q.-H.; Yan, F.; Xia, W.; Liu, C. Study of the coordinative nature of alkylaluminum modified Phillips CrO_x/SiO_2 catalyst by multinucleai solid-state NMR. *Pet. Sci.* **2013**, *10*, 577–583. [CrossRef]
32. Zhang, S.; Zhou, C.-A.; Wang, S.; Qin, Z.; Shu, G.; Wang, C.; Song, L.; Zheng, L.; Wei, X.; Ma, K.; et al. Facilitating CO_2 dissociation via Fe doping on supported vanadium oxides for intensified oxidative dehydrogenation of propane. *Chem. Eng. J.* **2024**, *481*, 148231. [CrossRef]
33. Ma, Z.; Xu, W.; Wang, Q.; Zhou, Q.; Zhou, J. Highly effective microwave catalytic oxidative dehydrogenation of propane by CO_2 over V-La-doped dendritic mesoporous silica-based microwave catalysts. *Chem. Eng. J.* **2022**, *435*, 135081. [CrossRef]
34. Zhang, Y.; Yu, Y.; Wang, R.; Dai, Y.; Bao, L.; Li, M.; Zhang, Y.; Liu, Q.; Xiong, D.; Wu, Q.; et al. Identifying the active site and structure-activity relationship in propane dehydrogenation over Ga_2O_3/ZrO_2 catalysts. *J. Catal.* **2023**, *428*, 115208. [CrossRef]
35. Shao, H.; Wang, X.; Gu, X.; Wang, D.; Jiang, T.; Guo, X. Improved catalytic performance of CrO_x catalysts supported on foamed Sn-modified alumina for propane dehydrogenation. *Micropor. Mesopor. Mater.* **2021**, *311*, 110684. [CrossRef]
36. Wang, J.; Song, Y.-H.; Liu, Z.-T.; Liu, Z.-W. Active and selective nature of supported CrO_x for the oxidative dehydrogenation of propane with carbon dioxide. *Appl. Catal. B Environ.* **2021**, *297*, 120400. [CrossRef]
37. Sun, G.; Huang, Q.; Li, H.; Liu, H.; Zhang, Z.; Wang, X.; Wang, Q.; Wang, J. Different supports-supported Cr-based catalysts for oxidative dehydrogenation of isobutane with CO_2. *Chin. J. Catal.* **2011**, *32*, 1424–1429. [CrossRef]
38. Scire, S.; Fiorenza, R.; Gulino, A.; Cristaldi, A.; Riccobene, P.M. Selective oxidation of CO in H_2-rich stream over ZSM5 zeolites supported Ru catalysts: An investigation on the role of the support and the Ru particle size. *Appl. Catal. A Gen.* **2016**, *520*, 82–91.
39. Zhang, S.; Ying, M.; Yu, J.; Zhan, W.; Wang, L.; Guo, Y.; Guo, Y. Ni_xAl1O_2-δ mesoporous catalysts for dry reforming of methane: The special role of $NiAl_2O_4$ spinel phase and its reaction mechanism. *Appl. Catal. B Environ.* **2021**, *291*, 120074. [CrossRef]
40. Karina Mathisen, D.G.N.; Andrew, M. Beale, Manuel Sanchez-Sanchez, Gopinathan Sankar, Wim Bras, and Serge Nikitenko. The selective catalytic reduction of NOx with CH_4 on Mn-ZSM5: A comparison with Co-ZSM5 and Cu-ZSM5. *Appl. Catal. B Environ.* **2007**, *111*, 3130–3138.
41. Liu, Z.; Zhang, F.; Rui, N.; Li, X.; Lin, L.; Betancourt, L.E.; Su, D.; Xu, W.; Cen, J.; Attenkofer, K.; et al. Highly active ceria-supported Ru catalyst for the dry reforming of methane: In situ identification of $Ru^{\delta+}$–Ce^{3+} interactions for enhanced conversion. *ACS Catal.* **2019**, *9*, 3349–3359. [CrossRef]
42. Shishido, T.; Shimamura, K.; Teramura, K.; Tanaka, T. Role of CO_2 in dehydrogenation of propane over Cr-based catalysts. *Catal. Today* **2012**, *185*, 151–156. [CrossRef]
43. Sokolov, S.; Stoyanova, M.; Rodemerck, U.; Linke, D.; Kondratenko, E.V. Comparative study of propane dehydrogenation over V-, Cr-, and Pt-based catalysts: Time on-stream behavior and origins of deactivation. *J. Catal.* **2012**, *293*, 67–75. [CrossRef]
44. Kresse, G.; Furthmuller, J. Efficient iterative schemes for ab initio total-energy calculations using a plane-wave basis set. *Phys. Rev. B* **1996**, *54*, 11169–11186. [CrossRef]

Disclaimer/Publisher's Note: The statements, opinions and data contained in all publications are solely those of the individual author(s) and contributor(s) and not of MDPI and/or the editor(s). MDPI and/or the editor(s) disclaim responsibility for any injury to people or property resulting from any ideas, methods, instructions or products referred to in the content.